Nano Research
2021, 14(9): 3267–3273
ISSN 1998-0124 CN 11-5974/O4
https://doi.org/10.1007/s12274-021-3517-6

Research Article

Mesoporous resin nanobowls with optimized donor–acceptor conjugation for highly efficient photocatalytic hydrogen peroxide production

Ling Yuan[1], Chaoqi Zhang[1], Jing Wang[1], Chao Liu[1] (✉), and Chengzhong Yu[1,2] (✉)

[1] School of Chemistry and Molecular Engineering, East China Normal University, Shanghai 200241, China
[2] Australian Institute for Bioengineering and Nanotechnology, The University of Queensland, Brisbane, Queensland 4072, Australia

Received: 16 January 2021 / **Revised:** 11 March 2021 / **Accepted:** 12 April 2021

ABSTRACT

Design of metal-free photocatalysts with customized chemical structure and nano-architecture is promising for photocatalytic hydrogen peroxide (H_2O_2) production. Herein, for the first time, mesoporous resorcinol–formaldehyde (MRF) nanobowls with optimized benzenoid–quinoid donor–acceptor (D–A) couples have been synthesized via an assembly–hydrothermal-etching process as high-performance photocatalysts for H_2O_2 production in a sacrificial agent-free system. At the hydrothermal temperature of ~ 250 °C, MRF-250 exhibits optimized structural features including a large surface area, suitable D–A couple ratio, enhanced light absorption, charge–hole separation and mass transfer. Thus, MRF-250 shows an unexpected H_2O_2 yield of 19.4 $mM \cdot g^{-1} \cdot h^{-1}$ in pure water, outperforming other RF samples prepared under different conditions and superior to most reported metal-free photocatalysts without the aid of sacrificial agents. Our work paves the way towards the elaborate design of highly effective metal-free photocatalysts for H_2O_2 production.

KEYWORDS

donor–acceptor couples, mesoporous, resin, photocatalysts, hydrogen peroxide

1 Introduction

Hydrogen peroxide (H_2O_2) is a valuable chemical with rapidly increasing demand in various important applications including organic synthesis, pulp and paper industry, environmental remediation and fuel cells [1]. The huge consumption of H_2O_2 (predicted to be 6.0 million tons by 2024) [2] requires efficient and low-cost production technology. Currently, anthraquinone oxidation is the predominant process for H_2O_2 synthesis, which involves multi-step organic reactions, large-scale infrastructure, high energy input and substantial waste generated [3, 4]. As one alternative route, direct synthesis from H_2 and O_2 in the presence of catalysts is more facile but exhibits a low selectivity and poor safety [5–8]. Therefore, developing efficient, economic and green routes for H_2O_2 production is of great significance.

Photocatalytic H_2O_2 production has emerged as a promisingly new approach, which only needs water and O_2 as raw materials, sustainable sunlight as energy supply and semiconductors as catalysts, without generating hazardous by-products. Great efforts have been devoted to designing promising photocatalysts, which is the key in determining the H_2O_2 production performance. Recent studies have demonstrated that metal-free photocatalysts such as graphitic carbon nitrides [9–12], covalent triazine frameworks [13], polymer-supported carbon dots [14] and graphene oxides [15] are promising photocatalysts for H_2O_2 production compared to inorganic metal-based photocatalysts [13]. However, metal-free photocatalysts generally possess wide bandgaps and respond to a limited region of the solar spectrum (< 460 nm) [16–18]. Another challenge is that most of the reported metal-free photocatalysts offer relatively low activity in the absence of organic sacrificial agents (e.g., ethonal, methanol, 2-propanol) [19–21]. Therefore, developing elabrately designed photocatalysts with suitable band gap and high activity in a sacrificial agent-free (e.g., pure water) system is highly desired.

Semiconductor polymers composed of electron donor (D) and acceptor (A) units play a crucial role in photovoltaic applications due to their highly tunable highest occupied/lowest unoccupied molecular orbital (HOMO/LUMO) energy levels and band gap by using different D–A combinations with distinct charge transfer interactions [22–24]. Very recently, the superior performance of D–A coupled polymer in photocatalytic H_2O_2 production was firstly demonstrated by Hirai and co-workers. Resorcinol–formaldehyde (RF) resins with benzenoid–quinoid D–A resorcinol couples with low-bandgaps and broad light absorbtion ranges (up to 700 nm) were designed, which exhibited a peak H_2O_2 yield of 2.8 $mM \cdot g^{-1} \cdot h^{-1}$ in a pure water system [25]. The optimized D/A ratio was demonstrated to be ~ 1, owing to the extended π-delocalization of D–A couple compared to single D or A. However, the solid and non-porous structure of RF resin spheres is adverse to the utilization of interior active sites, mass transfer and electron–hole pair separation during photocatalysis. Apart from the compositional design, architectural engineering towards delicate nanostructures is also highly important for enhancing photocatalytic performance, but rarely

Address correspondence to Chao Liu, cliu@chem.ecnu.edu.cn; Chengzhong Yu, czyu@chem.ecnu.edu.cn or c.yu@uq.edu.au

used in reported D–A coupled polymer photocatalysts [23]. It is expected that design of photocatalysts with highly active D–A couples (e.g., benzenoid–quinoid D–A couples) and a mesoporous structure and with large surface areas and accessible mesopores will increase the exposure of active sites, enhance charge separation and accelerate mass transfer [26], and thus the H_2O_2 production performance will be improved.

Herein, for the first time, bowl-like mesoporous RF (MRF) nanoparticles with the D–A couple were prepared as a photocatalyst for H_2O_2 production in water. The synthesis process of MRF materials is illustrated in Scheme 1. Using resorcinol, formaldehyde and tetrapropyl orthosilicate (TPOS) as precursors, SiO_2 core particles, SiO_2 primary particles and RF oligomers were firstly assembled [27]. The SiO_2 primary particles and RF oligomers co-condense onto SiO_2 core particles, forming SiO_2@RF composite spheres in step (1). Through further hydrothermal treatment at different temperatures (T) such as 250 °C (the optimized temperature), benzenoid–quinoid D–A couples are generated in the RF framework, resulting in SiO_2@RF-250 in step (2). Finally, MRF-250 is yielded in step (3), during which the D–A coupled structure with well retained mesoporous structure is produced after silica removal. The resultant MRF-250 exhibits a uniform nanobowl morphology with a large surface area of 101.0 $m^2 \cdot g^{-1}$, a mesopore size of ~ 10 nm, an optimized A/D molar ratio of 0.9:1, enhanced light absorption, charge separation and mass transfer. Combining all these merits, MRF-250 delivers an excellent photocatalytic H_2O_2 yield of 19.4 $mM \cdot g^{-1} \cdot h^{-1}$, outperforming other counterparts prepared under different conditions and even superior to most reported metal-free photocatalysts.

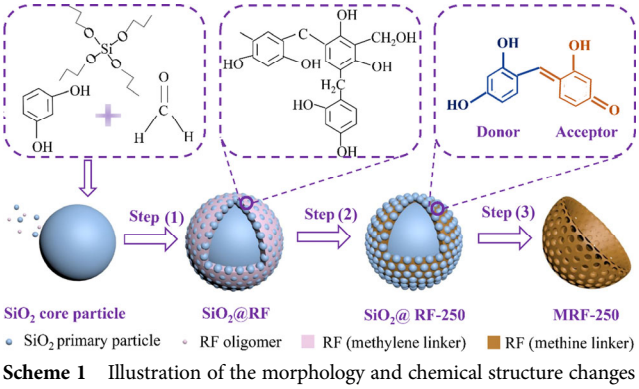

Scheme 1 Illustration of the morphology and chemical structure changes during the synthesis process of MRF-250

2 Experimental

2.1 Chemicals

TPOS was purchased from Tokyo Chemical Industry UK Ltd. 30% H_2O_2 aqueous solution, acetone and hydrofluoric acid (HF) were obtained from Sinopharm Chemical Regent Co., Ltd. Resorcinol (Adamas), formaldehyde (Adamas), ethanol (Adamas), and ammonium hydroxide ($NH_3 \cdot H_2O$) (Adamas) were used as received without further purification. Milli-Q water was used in all experiments.

2.2 Methods

2.2.1 *Synthesis of SiO2@RF precursor*

The SiO_2@RF composite was synthesized according to our reported work [27]. Typically, TPOS (3.5 mL) was added to the solution containing ethanol (70 mL), H_2O (10 mL), and $NH_3 \cdot H_2O$ (3 mL, 25 wt.%) under stirring at room temperature. After 15 min, resorcinol (0.4 g) and formaldehyde (0.56 mL, 37 wt.%) were added to the solution with reaction for 24 h, generating the SiO_2@RF precursor solution for further use.

2.2.2 *Synthesis of RF bowls*

The SiO_2@RF precursor solution was transferred to a Teflon-lined stainless-steel autoclave and left in an oven for hydrothermal treatment at different temperatures for 24 h. The formed solid was washed thoroughly with acetone and dried in vacuum at room temperature for 12 h, named as SiO_2@RF-T (T represents the hydrothermal temperature, T = 150, 200, 250, and 270 °C). After removal of silica by HF, products with different D/A ratios were fabricated (denoted as MRF-T). For comparison, SiO_2@RF composite without hydrothermal treatment was also etched by HF, resulting in MRF. A solid RF sample was fabricated using the similar process of MRF-250, except without adding TPOS (named as SRF-250).

2.3 Characterization

Powder X-ray powder diffraction (XRD) patterns were recorded by using a Bruker D8 Advanced X-ray diffractometer with Cu Kα radiation (λ = 0.154 nm). Fourier transform infrared spectroscopy (FTIR) spectra were recorded on a Thermal-Nicolet iS50 spectrometer. Diffuse reflectance ultraviolet–visible (UV–vis) absorption spectroscopy was performed on a UV–vis spectrophotometer (Lambda950) with $BaSO_4$ as a reference material. UV–vis spectra were obtained by using a UV–vis spectrophotometer (BioTek Synergy H1 Hybrid Multi-Mode Monochromator). Transmission electron microscopy (TEM) images were collected on a JEM-2100F (JEOL, Japan) with an acceleration voltage of 200 kV. Scanning electron microscope (SEM) images were obtained using a Zeiss Gemini 450 field emission SEM. The solid-state nuclear magnetic resonances (NMR) spectra of ^{13}C were collected on a Bruker BioSpin Avance III HD 400 high performance digital NMR spectrometer from Switzerland. Electron spin resonance (ESR) spectra were recorded on a Bruker A300 ESR spectrometer. Thermogravimetric analysis (TGA) was conducted on a Mettler-Toledo TGA/SDTA851e equipment.

2.4 Calculation of D/A molar ratio

The mole ratios of the quinoid and benzenoid units in the resins were calculated from the deconvoluted peak areas in ^{13}C-NMR spectrum, by using the following two equations

$$\text{Quinoid}\ (\%) = \frac{[\text{quinone C=O carbon (b)} \times 6 \times 100]}{[\text{all aromatic carbons (b,c,d,f,g,h)}]} \times 100 \quad (1)$$

$$\text{Benzenoid}\% = 100\% - \text{quinoid}\% \quad (2)$$

2.5 Photogeneration of H_2O_2

To measure the reductive conversion of O_2 into H_2O_2, 50 mg of photocatalyst was dispersed in 30 mL of deionized water by sonification for 5 min. After O_2 bubbling for 1 h, the photoreaction was initiated by irradiation of a 300 W xenon lamp (λ > 420 nm). At given time intervals, a certain suspension was collected and filtrated with a millipore filter (0.45 μm) to remove the photocatalyst. The H_2O_2 concentration was determined by iodometry [28]. Typically, 100 μL of reaction solution was added to 2 mL mixture solution of 0.05 M potassium hydrogen phthalate ($C_8H_5KO_4$) and 0.2 M potassium iodide (KI) with reaction for 30 min. Under acidic condition, the H_2O_2 molecules would react with I^- to generate I^{3-}. The amount of I^{3-} was measured by a UV spectrophotometer

at 350 nm, which was further used to quantify the generated H_2O_2.

2.5.1 *Solar energy to H_2O_2 conversion efficiency*

To determine the solar energy to H_2O_2 conversion efficiency, the H_2O_2 production by photocatalysis was conducted following the same procedure mentioned above except using 5 mg·mL^{-1} photocatalyst and AM1.5G simulated sunlight (λ > 420 nm). The light intensity was determined with a radiometer (Perfect Light, PL-MW2000). The total input power was determined to be 0.432 W. The solar-to-chemical conversion (SCC) is calculated from the following equation

$$\text{SCC}\ (\%) = \frac{[\Delta G \text{ for } H_2O_2 \text{ generation } (\text{J}\cdot\text{mol}^{-1})][H_2O_2\ (\text{mol})]}{[\text{total input power (W)}][\text{reaction time (s)}]} \times 100 \quad (3)$$

2.5.2 *Apparent quantum yield (AQY)*

The AQY was measured at selected light lengths including 365, 450, 550, and 600 nm. The total input powers were determined to be 0.123, 0.146, 0.196, and 0.225 W, respectively. AQY was calculated using the following equation

$$\text{AQY}\ (\%) = \frac{[\text{the number of evolved } H_2O_2 \text{ molecules} \times 2]}{\text{photon number}} \times 100 \quad (4)$$

2.6 Photoelectrochemical test

The photocurrent test was carried out on a Chenhua CHI 760E electrochemical workstation with a standard three-electrode cell system in 0.1 M Na_2SO_4 electrolyte using Ag/AgCl electrode, Pt wire and catalyst/indium-doped tin oxide (ITO) as the reference, counter and working electrodes, respectively. The working electrode was prepared as follows: 5 mg of the sample was uniformly dispersed in 30 μL of 10% nafion solution to produce a slurry. Then, the slurry was coated onto an ITO glass (effective area: 1 cm^2) and dried at 60 °C for 12 h. For transient photocurrent test, a 300 W xenon lamp (PLS- SXE300D/300 DUV, Perfect Light) equipped with a 420 nm cutoff filter was utilized as the light source. Electrochemical impedance spectroscopy (EIS) was recorded in the frequency range of 1,000 kHz–0.01 Hz under irradiation.

3 Results and discussion

SEM and TEM were employed to investigate the morphologies of samples obtained at different stages. SiO_2@RF shows a uniform spherical morphology with an average diameter of ~ 400 nm and a solid structure (Figs. S1(a)–S1(c) in the Electronic Supplementary Material (ESM)). After hydrothermal treatment at 250 °C, the diameter of SiO_2@RF-250 (Figs. S1(d)–S1(f) in the ESM) slightly increases to 450 nm. Silica nano-spikes with higher contrast are observed to be embedded in the RF matrix with a lower contrast on the outer region. The slightly increased particle size of SiO_2@RF-250 compared to SiO_2@RF may be ascribed to the further growth of residual RF precursors (Fig. S2 in the ESM) during hydrothermal process. After removal of RF from SiO_2@RF-250 by calcination in air, the resultant SiO_2 nanoparticle (denoted as SiO_2-250) exhibits a core–shell structure with solid core of an average diameter of ~ 350 nm and a radial porous shell of a thickness of ~ 50 nm (Figs. S3(a) and S3(b) in the ESM). The diameter of the SiO_2 spikes on the shell is measured to be ~ 10 nm (Fig. S3(c) in the ESM). The above results are consistent with the core–shell structure of SiO_2@RF-250 shown in Scheme 1.

Removing SiO_2 from SiO_2@RF-250 composite finally results in the formation of MRF-250. The total removal of silica is confirmed by TGA curve of MRF-250, in which 100% of weight loss is observed at ~ 600 °C due to the complete decomposition of RF resin (Fig. S4 in the ESM). The SEM image (Fig. 1(a)) shows highly dispersed nanoparticles with a distinctive bowl-like morphology and average diameter of ~ 400 nm. In the enlarged SEM image of a typical particle (Fig. 1(b)), deformed shell and relatively smooth surface are observed. TEM images in Figs. 1(c) and 1(d) further demonstrate the uniform nanobowl structure of MRF-250, in agreement with the SEM observations. The relatively lower contrast in the center region than outer shell further indicates the concaved structure [29]. At higher magnifications (Figs. 1(e) and 1(f)), large amount of mesopores with diameter of ~ 10 nm are clearly found, which are distributed through the whole skeleton of MRF-250.

The mesoporous structure is further evidenced by the N_2 adsorption–desorption isotherm (Fig. 1(g)), in which a typical type IV hysteresis loop is exhibited in high relative pressure regions (P/P_0 of 0.75–1.0), suggesting the existence of abundant mesopores. The Brunauer–Emmett–Teller (BET) surface area and pore volume are measured to be 101.0 m^2·g^{-1} and 0.33 cm^3·g^{-1}. The pore diameter distribution curve calculated from the adsorption branch by Barrett–Joyner–Halenda (BJH) model shows that the mesopore size centers at ~ 10 nm (Fig. 1(f)), in accordance with the TEM results. The mesopore size also matches with the size of shell SiO_2 particle in SiO_2-250, further supporting the formation mechanism of MRF-250 shown in Scheme 1.

The effect of hydrothermal temperature on the structure of MRF-T was then carefully investigated (T = 150, 200, and 270 °C). MRF was also synthesized by directly removing silica from SiO_2@RF. As shown in Fig. S5 in the ESM, all the RF samples possess bowl-like morphology with more deformation at increasing hydrothermal temperature, which may be ascribed to the higher degree of polymerization and shrinkage at higher temperature. The N_2 isotherms of MRF, MRF-150 and MRF-200 show type I hysteresis loop, different from MRF-250 (Fig. S6(a) in the ESM). Meanwhile, no obvious peaks are found in the range of mesopores pore size distribution curves (Fig. S6(b) in the ESM). This may be ascribed to that the RF framework obtained at a relatively lower hydrothermal temperature is not

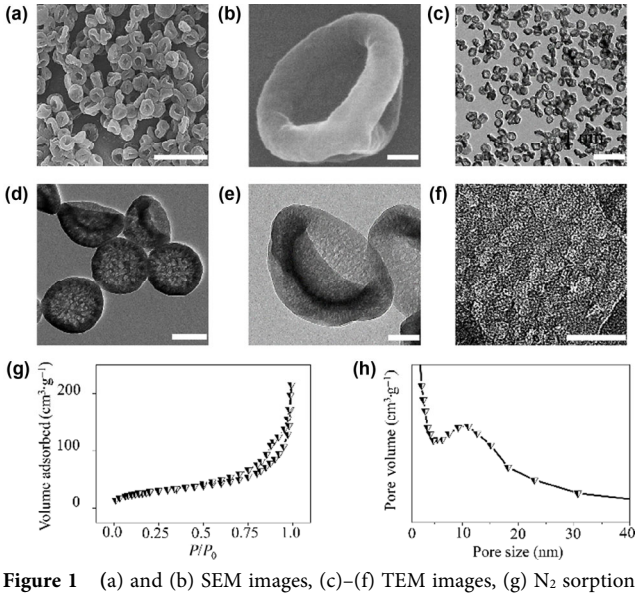

Figure 1 (a) and (b) SEM images, (c)–(f) TEM images, (g) N_2 sorption isotherms and (h) pore size distribution curves of MRF-250. Scale bars are (a) and (c) 1 μm, (d) 200 nm, (b) and (e) 100 nm, and (f) 50 nm, respectively.

rigid enough to maintain the mesoporous structure during silica removing, thus resulting in extremely low BET surface area and pore volume (Table S1 in the ESM). At a higher hydrothermal temperature, MRF-270 possesses a similar mesoporous structure to MRF-250 with slightly lower surface area and pore volume. In addition, SRF-250 is also prepared by using the similar synthesis protocol of MRF except without adding TPOS (Fig. S7 in the ESM). Through hydrothermal treatment at 250 °C, SRF-250 is obtained, showing a solid and dense structure with a low surface area of 27 $m^2 \cdot g^{-1}$ and a pore volume of 0.06 $cm^3 \cdot g^{-1}$.

The various carbon structures in RF resins were investigated by solid-state ^{13}C NMR technique. The NMR spectrum of MRF-250 is presented in Fig. 2(a), which can be fitted into 14 carbon components (a–n in Fig. 2(b)), and assigned to aromatics, linkers and residual groups in RF resins [25]. Specifically, the peaks at 182 ppm (b in Fig. 2(a)) and 126 ppm (e in Fig. 2(a)) are assigned to the quinone C=O carbon [30] of the quinoid units (A) and the corresponding methine linker carbon [31] with almost the same peak areas. This observation indicates the formation of quinoid units π-conjugated with benzenoid units via methine linkers according to a previous report [25]. Furthermore, the D/A molar ratios in different RF samples are calculated by integration of the a–n components in the spectra for the respective resins (Fig. S8 in the ESM). As summarized in Fig. 2(c), the A/D ratio increases from 0.3:1.0 to 1.4:1 by increasing the hydrothermal temperature from 150 to 270 °C. At the same hydrothermal temperature, the A/D ratio of SRF-250 is almost same with MRF-250 (~ 0.9:1.0), close to the optimized D/A coupling ratio of 1.

The chemical structures of different RF materials were further studied by FTIR (Fig. S9 in the ESM). The spectrum of MRF exhibits bands at 1,615, 1,450, and 1,303 cm^{-1}, are assigned to C=C group of aromatic ring, C–H group of methylene linker, and C–H group of aromatic ring, consistent with the reported RF material synthesized at room temperature [32]. With increasing the hydrothermal temperature to 250 and 270 °C, a new peak of quinone group is observed at 1,650 cm^{-1} in the spectra of MRF-250, 270 and SRF-250. Meanwhile, the band intensities of aromatic ring (C=C) and methylene linker (C–H) groups increase, indicating the formation of methine linkers according to the previous reports [25, 33].

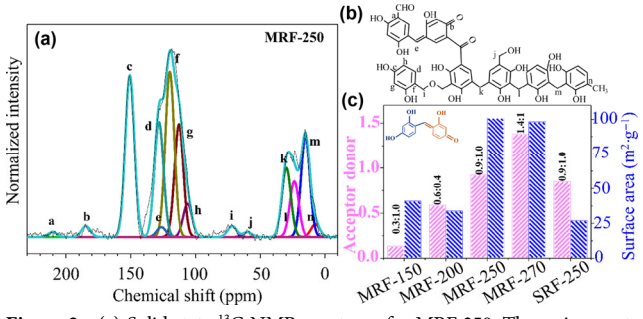

Figure 2 (a) Solid-state ^{13}C-NMR spectrum for MRF-250. The assignments of the respective carbon components: aldehyde –CHO (210 ppm: a), quinone C=O (182 ppm: b), resorcinol C–OH (153 ppm: c), non-substituted resorcinol C at the meta position (130 ppm: d), methine linker –C= (126 ppm: e), substituted resorcinol C (117 ppm: f), non-substituted resorcinol C at the para and ortho positions (110 ppm: g, 105 ppm: h), methylene ether linker –C–O–C– (70 ppm: i), methylol C–OH (55 ppm: j), methylene linker –C– substituted to 4,4'-, 2,4'-, and 2,2'-positions of resorcinols (30 ppm: k, 20 ppm: l, 10 ppm: m), and methyl –CH_3 (5 ppm: n). (b) The possible chemical structure of MRF-250. (c) The A/D ratio and BET surface areas of MRF-150, MRF-200, MRF-250, MRF-270 and SRF-250. The mole fractions of the quinoid and benzenoid units in the resins were determined from ^{13}C-NMR spectrum.

The XRD patterns of different RF resins are shown in Fig. S10 in the ESM. All resins exhibit broad diffraction at 2θ = ~ 20°, originated from the π-stacking interaction between D–A couples. It can be also found that this diffraction shifts to higher degrees for the resins prepared at higher hydrothermal temperatures, implying a narrowed distance between the aromatic planes with stronger π-stacking [25]. Together with the NMR and FTIR results, the formation of D–A coupled MRF-250 with a D/A coupling ratio close to 1 is demonstrated.

The photocatalytic activities of synthesized catalysts for H_2O_2 production are evaluated under visible-light irradiation without using sacrificing electron donors (Fig. 3(a)). The time-dependent change in the amounts of generated H_2O_2 is shown in Fig. 3(a). MRF exhibits poor activity with H_2O_2 production of 7.2 μmol after reaction for 120 min. Through hydrothermal treatment, the H_2O_2 production amount gradually increases from 19.2 to 58.4 μmol with temperature increasing from 150 to 250 °C. When the temperature is further raised to 270 °C, less H_2O_2 amount of 43.3 μmol is generated. Therefore, the optimized H_2O_2 production activity is achieved by MRF-250, also superior to SRF-250 that produces 29.7 μmol of H_2O_2 in 120 min, indicating the positive contribution of both D–A couples and mesopores during photocatalysis. Notably, MRF-250 delivers a H_2O_2 production rate of 19.4 $mM \cdot g^{-1} \cdot h^{-1}$, which is higher than most reported sacrificing electron donor-free systems, even comparable to the best catalysts using sacrificial agents (Fig. 3(c) and Table S2 in the ESM) [12, 13, 19, 20, 25, 34–40]. By prolonging the reaction time to 24 h, the H_2O_2 generation amount of MRF-250 increases to 169.2 μmol (Fig. S11 in the ESM), higher than that of SRF-250 (106.2 μmol), indicating the sustainable production of H_2O_2.

Generally, the concentration of H_2O_2 is determined by the competition between the H_2O_2 formation (k_f) and decomposition (k_d) rates over the catalysts, which can be calculated based on the following formula $[H_2O_2] = (k_f/k_d)(1 - \exp(-k_d \cdot t))$ [11]. As shown in Fig. 3(b), MRF-250 exhibits the highest k_f and lowest k_d among all samples. In addition, the photocatalytic

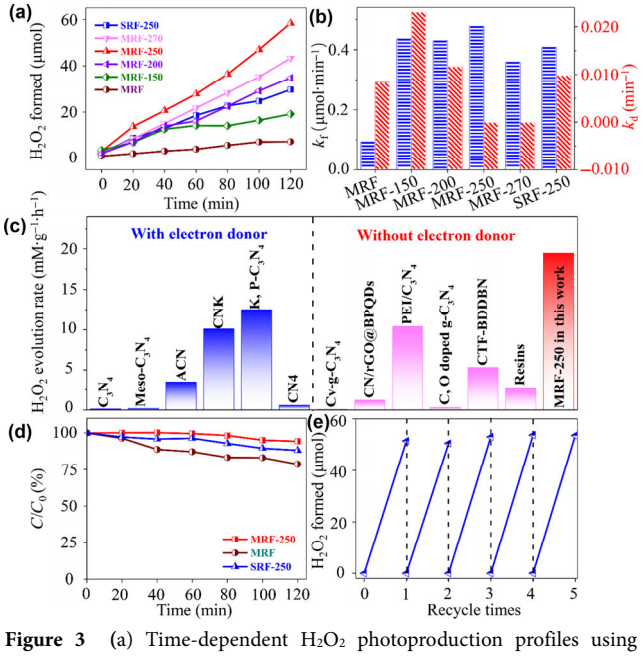

Figure 3 (a) Time-dependent H_2O_2 photoproduction profiles using various RF photocatalysts. (b) The H_2O_2 formation rate constant (k_f, blue) and H_2O_2 decomposition rate constant (k_d, red) of various RF photocatalysts. (c) Comparison of H_2O_2 production rate with reported photocatalysts. (d) The photocatalytic decomposition of H_2O_2 (0.1 mM) for MRF-250, MRF, and SRF-250 under visible light irradiation. (e) Reusability of MRF-250 for H_2O_2 production.

decomposition of H_2O_2 was also measured [41] by using the 0.1 mM H_2O_2 aqueous solution as origin reaction solution. As shown in Fig. 3(d), 10% and 20% of H_2O_2 are decomposed after 120 min by SRF-250 and MRF respectively, but only 6% of H_2O_2 is decomposed by MRF-250. Therefore, MRF-250 not only promotes the production of H_2O_2 but also prevents the subsequent decomposition of H_2O_2 under irradiation.

The SCC efficiency of MRF-250 was tested under AM1.5G simulated sunlight ($\lambda > 420$ nm) according to the previous report [25]. As shown in Fig. S12 in the ESM, the SCC efficiency for H_2O_2 generation is 0.84% after 1 h of photoirradiation, then gradually decreases to 0.33% at 5 h of photoirradiation. Further prolonging the reaction time to 8 h results in an SCC efficiency of 0.31% without significant decrease. The sample after reaction for 4 h was collected and characterized by the NMR and FTIR (Figs. S13 and S14 in the ESM). The ketone carbon (in Fig. S13 in the ESM) at 190 ppm is found, but not in the fresh MRF-250, suggesting the resin oxidation may consume the photogenerated holes and promote electron–hole separation for O_2 reduction into H_2O_2 [25]. This is evidenced by the decreased SCC efficiency of reused MRF-250, the value of which is ~ 0.32% at 1 h, lower than that of fresh MRF-250 (0.84%, Fig. S15 in the ESM). However, this contribution is expected to decrease when available sites of resin (e.g., methylol and methylene groups) are oxidized, leading to gradually decreased SCC efficiency with prolonged reaction time. The higher SCC efficiency decrease of MRF-250 than reported RF [25] may be ascribed to the high specific surface area of MRF-250 with more surface exposed functional groups that can be oxidized.

In addition, from the NMR spectrum the peak of quinone group at 182 ppm is observed and the A/D ratio is calculated to be ~ 0.88:1, similar to that of fresh MRF-250 (0.9:1). In the FTIR spectra of MRF-250 after reaction for 4 h, the peak of quinone group is also observed at ~ 1,650 cm^{-1}. Therefore, the SCC efficiency change as a function of time should be mainly attributed to the resin self-oxidation, instead of the D–A couple structure.

To evaluate the effect of light condition on the H_2O_2 production, the AQY of MRF-250 was measured with four wavelengths (Fig. S16 in the ESM). The AQY reached the peak value of 2.9% at 365 nm and decreased to 2.5%, 1.0% and 0.3% at 450, 550 and 600 nm, respectively, which is in accordance with the absorption spectrum of MRF-250.

The cycling performance of MRF-250 was then determined. As shown in Fig. 3(e), after recycled for five times under the same conditions, MRF-250 shows negligible changes of the catalytic performance with 98% of H_2O_2 amount generated compared to the first cycle, indicating its robust activity. In addition, the TEM image of MRF-250 (Fig. S17 in the ESM) after use shows well-retained mesoporous structure and bowl-like morphology.

To gain insight into the enhanced activity of MRF-250, the semiconductive properties were further studied. The UV–vis absorption spectra of different RF photocatalysts are shown in Fig. 4(a). MRF exhibits relatively low absorption in the range of visible light. With the hydrothermal temperature rising, the absorption is enhanced first and then reduced, and reaches the peak at 250 °C due to the optimized D/A ratio (close to 1) in MRF-250, which can extend the π-delocalization and reduce the band gap according to a previous report [25]. Compared to SRF-250 with almost the same D/A ratio, MRF-250 also shows enhanced light absorption. This may be ascribed to that the created mesopores in MRF-250 with high surface area promote the exposure and utilization of D–A couples, thus resulting in the superior light harvesting ability.

To investigate the separation and transfer behaviors of charge carries, transient photocurrent responses and EIS were also tested. Within the light on/off cycles, the generated photocurrent intensity first increases and then decreases when the hydrothermal temperature increases (Fig. 4(b)). Among different MRF samples, MRF-250 delivers the largest photocurrent, which is also ~ 2 times higher than SRF-250, suggesting the highest separation efficiency of electrons and holes. The EIS spectra (Fig. 4(c)) show that MRF-250 presents the smallest semicircle diameter, indicating the lowest charge transfer resistance.

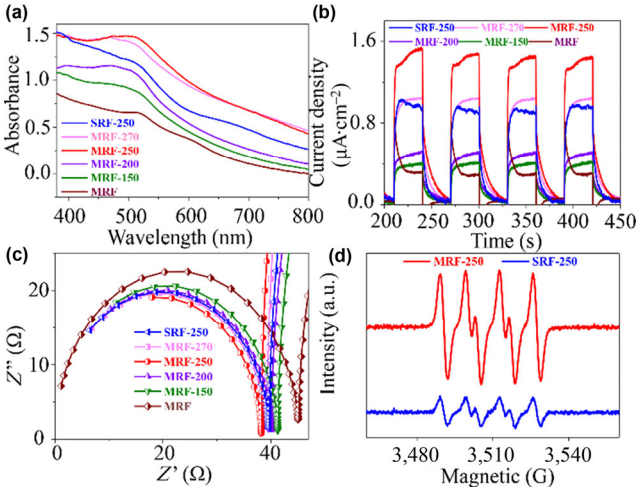

Figure 4 (a) UV–vis absorption spectra. (b) Transient photocurrent responses and (c) EIS profiles of different RF photocatalysts. (d) ESR signals of DMPO-·O_2^- over MRF-250 and SRF-250 under visible light.

To get insights on the mechanism of photocatalytic H_2O_2 production of MRF-250 and SRF-250, the 5,5-dimethyl-pyrroline N-oxide (DMPO) spin-trapping ESR technique was employed for the detection of $\cdot O_2^-$. As shown in Fig. 4(d), characteristic peaks assigned to DMPO-·O_2^- are observed, indicating the generation of $\cdot O_2^-$ during the photocatalytic reaction. Therefore, the H_2O_2 production on MRF-250 is likely through a two-step single-electron reduction mechanism with $\cdot O_2^-$ as the intermediate product ($O_2 + e^- \rightarrow \cdot O_2^-$ and $\cdot O_2^- + 2H^+ + e^- \rightarrow H_2O_2$) [12, 34]. In addition, the signal intensities in the spectrum of MRF-250 are stronger than those of SRF-250, further confirming the enhanced activity of MRF-250.

Based on the aforementioned observations, the excellent photocatalytic performance of MRF-250 may be attributed to following reasons: (1) The optimized ratio of D–A couple (close to 1:1) extends the π-delocalization, enhances the light absorption and produces large amount of charge carries under irradiation; (2) the mesoporous and concaved bowl-like structure accelerates the charge transfer to the surface of catalyst, and promotes the charge separation. Meanwhile, the further reaction with produced H_2O_2 is disadvantaged, thus preventing the subsequent decomposition of H_2O_2; (3) the mesoporous structure with high surface area also increases the exposure of active sites and facilitates the adsorption of reactants and desorption of products, thus accelerating the photocatalytic reaction.

4 Conclusion

In summary, we report the synthesis of MRF nanobowls with optimized benzenoid–quinoid donor–acceptor (D–A) couples as efficient photocatalysts through an assembly–hydrothermal-etching process for H_2O_2 production in a pure water system. The hydrothermal temperature is optimized to be ~ 250 °C for obtaining MRF-250 with large surface area, suitable D–A couple ratio, enhanced light absorption, charge separation and mass

transfer. Benefiting from these structural advantages, MRF-250 exhibits the highest H_2O_2 yield of 19.4 $mM \cdot g^{-1} \cdot h^{-1}$ among all prepared samples, which is even superior to reported metal-free photocatalysts without the usage of sacrificial agents.

Acknowledgements

We acknowledge support from the National Natural Science Foundation of China (Nos. 21905092, 51908218, and 22075085), Shanghai Science and Technology Foundation (No. 19JC1412100), China Postdoctoral Science Foundation (Nos. 2020T130196, and 2019M651426) and the Fundamental Research Funds for the Central Universities.

Electronic Supplementary Material: Supplementary material (preparation of resorcinol–formaldehyde nanobowls and their structural and photocatalytic characterizations including the optical image, SEM, TEM images, BET test, TGA, NMR, FTIR and XRD measurements) is available in the online version of this article at https://doi.org/10.1007/s12274-021-3517-6.

References

[1] Sun, Y. Y.; Han, L.; Strasser, P. A comparative perspective of electrochemical and photochemical approaches for catalytic H_2O_2 production. *Chem. Soc. Rev.* **2020**, *49*, 6605–6631.

[2] Melchionna, M.; Fornasiero, P.; Prato, M. The rise of hydrogen peroxide as the main product by metal-free catalysis in oxygen reductions. *Adv. Mater.* **2019**, *31*, 1802920.

[3] Campos-Martin, J. M.; Blanco-Brieva, G.; Fierro, J. L. Hydrogen peroxide synthesis: An outlook beyond the anthraquinone process. *Angew. Chem., Int. Ed.* **2006**, *45*, 6962–6984.

[4] Cai, J. S.; Huang, J. Y.; Wang, S. C.; Iocozzia, J.; Sun, Z. T.; Sun, J. Y.; Yang, Y. K.; Lai, Y. K.; Lin, Z. Q. Crafting mussel-inspired metal nanoparticle-decorated ultrathin graphitic carbon nitride for the degradation of chemical pollutants and production of chemical resources. *Adv. Mater.* **2019**, *31*, 1806314.

[5] Kim, H. I.; Choi, Y.; Hu, S.; Choi, W.; Kim, J. H. Photocatalytic hydrogen peroxide production by anthraquinone-augmented polymeric carbon nitride. *Appl. Catal. B: Environ.* **2018**, *229*, 121–129.

[6] Edwards, J. K.; Solsona, B.; Ntainjua, N. E.; Carley, A. F.; Herzing, A. A.; Kiely, C. J.; Hutchings, G. J. Switching off hydrogen peroxide hydrogenation in the direct synthesis process. *Science* **2009**, *323*, 1037–1041.

[7] Choi, C. H.; Kim, M.; Kwon, H. C.; Cho, S. J.; Yun, S.; Kim, H. T.; Mayrhofer, K. J.; Kim, H.; Choi, M. Tuning selectivity of electrochemical reactions by atomically dispersed platinum catalyst. *Nat. Commun.* **2016**, *7*, 10922.

[8] Edwards, J. K.; Ntainjua N. E.; Carley, A. F.; Herzing, A. A.; Kiely, C. J.; Hutchings, G. J. Direct synthesis of H_2O_2 from H_2 and O_2 over gold, palladium, and gold–palladium catalysts supported on acid-pretreated TiO_2. *Angew. Chem., Int. Ed.* **2009**, *48*, 8512–8515.

[9] Wang, K. F.; Shao, D. K.; Zhang, L.; Zhou, Y. Y.; Wang, H. P.; Wang, W. Z. Efficient piezo-catalytic hydrogen peroxide production from water and oxygen over graphitic carbon nitride. *J. Mater. Chem. A* **2019**, *7*, 20383–20389.

[10] Zheng, Y.; Yu, Z. H.; Ou, H. H.; Asiri, A. M.; Chen, Y. L.; Wang, X. C. Black phosphorus and polymeric carbon nitride heterostructure for photoinduced molecular oxygen activation. *Adv. Funct. Mater.* **2018**, *28*, 1705407.

[11] Zhang, P.; Tong, Y. W.; Liu, Y.; Vequizo, J. J. M.; Sun, H. W.; Yang, C.; Yamakata, A.; Fan, F. T.; Lin, W.; Wang, X. C. et al. Heteroatom dopants promote two-electron O_2 reduction for photocatalytic production of H_2O_2 on polymeric carbon nitride. *Angew. Chem., Int. Ed.* **2020**, *59*, 16209–16217.

[12] Yang, Y.; Zeng, G. M.; Huang, D. L.; Zhang, C.; He, D. H.; Zhou, C. Y.; Wang, W. J.; Xiong, W. P.; Li, X. P.; Li, B. S. et al. Molecular engineering of polymeric carbon nitride for highly efficient photocatalytic oxytetracycline degradation and H_2O_2 production. *Appl. Catal. B: Environ.* **2020**, *272*, 118970.

[13] Chen, L.; Wang, L.; Wan, Y. Y.; Zhang, Y.; Qi, Z. M.; Wu, X. J.; Xu, H. X. Acetylene and diacetylene functionalized covalent triazine frameworks as metal-free photocatalysts for hydrogen peroxide production: A new two-electron water oxidation pathway. *Adv. Mater.* **2020**, *32*, 1904433.

[14] Gogoi, S.; Karak, N. Solar-driven hydrogen peroxide production using polymer-supported carbon dots as heterogeneous catalyst. *Nano-Micro Lett.* **2017**, *9*, 40.

[15] Hou, W. C.; Wang, Y. S. Photocatalytic generation of H_2O_2 by graphene oxide in organic electron donor-free condition under sunlight. *ACS Sustainable Chem. Eng.* **2017**, *5*, 2994–3001.

[16] Martin, D. J.; Qiu, K. P.; Shevlin, S. A.; Handoko, A. D.; Chen, X. W.; Guo, Z. X.; Tang, J. W. Highly efficient photocatalytic H_2 evolution from water using visible light and structure-controlled graphitic carbon nitride. *Angew. Chem., Int. Ed.* **2014**, *53*, 9240–9245.

[17] Zhang, J. S.; Wang, X. C. Solar water splitting at λ = 600 nm: A step closer to sustainable hydrogen production. *Angew. Chem., Int. Ed.* **2015**, *54*, 7230–7232.

[18] Wang, Y. O.; Silveri, F.; Bayazit, M. K.; Ruan, Q. S.; Li, Y. M.; Xie, J. J.; Catlow, C. R. A.; Tang, J. W. Bandgap engineering of organic semiconductors for highly efficient photocatalytic water splitting. *Adv. Energy Mater.* **2018**, *8*, 1801084.

[19] Zeng, X. K.; Liu, Y.; Kang, Y.; Li, Q. Y.; Xia, Y.; Zhu, Y. L.; Hou, H. L.; Uddin, M. H.; Gengenbach, T. R.; Xia, D. H. et al. Simultaneously tuning charge separation and oxygen reduction pathway on graphitic carbon nitride by polyethylenimine for boosted photocatalytic hydrogen peroxide production. *ACS Catal.* **2020**, *10*, 3697–3706.

[20] Shiraishi, Y.; Kanazawa, S.; Sugano, Y.; Tsukamoto, D.; Sakamoto, H.; Ichikawa, S.; Hirai, T. Highly selective production of hydrogen peroxide on graphitic carbon nitride (g-C_3N_4) photocatalyst activated by visible light. *ACS Catal.* **2014**, *4*, 774–780.

[21] Fu, Y. J.; Liu, C. A.; Zhang, M. L.; Zhu, C.; Li, H.; Wang, H. B.; Song, Y. X.; Huang, H.; Liu, Y.; Kang, Z. H. Photocatalytic H_2O_2 and H_2 generation from living *Chlorella vulgaris* and carbon micro particle comodified g-C_3N_4. *Adv. Energy Mater.* **2018**, *8*, 1802525.

[22] Zhao, F. W.; Wang, C. R.; Zhan, X. W. Morphology control in organic solar cells. *Adv. Energy Mater.* **2018**, *8*, 1703147.

[23] Dang, D. F.; Yu, D. H.; Wang, E. G. Conjugated donor–acceptor terpolymers toward high-efficiency polymer solar cells. *Adv. Mater.* **2019**, *31*, 1807019.

[24] Kang, T. E.; Kim, K. H.; Kim, B. J. Design of terpolymers as electron donors for highly efficient polymer solar cells. *J. Mater. Chem. A* **2014**, *2*, 15252–15267.

[25] Shiraishi, Y.; Takii, T.; Hagi, T.; Mori, S.; Kofuji, Y.; Kitagawa, Y.; Tanaka, S.; Ichikawa, S.; Hirai, T. Resorcinol–formaldehyde resins as metal-free semiconductor photocatalysts for solar-to-hydrogen peroxide energy conversion. *Nat. Mater.* **2019**, *18*, 985–993.

[26] Huang, X. X.; Shen, T.; Zhang, T.; Qiu, H. L.; Gu, X. X.; Ali, Z.; Hou, Y. L. Efficient oxygen reduction catalysts of porous carbon nanostructures decorated with transition metal species. *Adv. Energy Mater.* **2020**, *10*, 1900375.

[27] Zhang, H. W.; Noonan, O.; Huang, X. D.; Yang, Y. N.; Xu, C.; Zhou, L.; Yu, C. Z. Surfactant-free assembly of mesoporous carbon hollow spheres with large tunable pore sizes. *ACS Nano* **2016**, *10*, 4579–4586.

[28] Wei, Z.; Liu, M. L.; Zhang, Z. J.; Yao, W. Q.; Tan, H. W.; Zhu, Y. F. Efficient visible-light-driven selective oxygen reduction to hydrogen peroxide by oxygen-enriched graphitic carbon nitride polymers. *Energy Environ. Sci.* **2018**, *11*, 2581–2589.

[29] Wang, N.; Cheng, G.; Guo, L. P.; Tan, B.; Jin, S. B. Hollow covalent triazine frameworks with variable shell thickness and morphology. *Adv. Funct. Mater.* **2019**, *29*, 1904781.

[30] Liebscher, J.; Mrówczyński, R.; Scheidt, H. A.; Filip, C.; Hădade, N. D.; Turcu, R.; Bende, A.; Beck, S. Structure of polydopamine: A never-ending story? *Langmuir* **2013**, *29*, 10539–10548.

[31] del Valle, M. A.; Herrera, F. V.; Díaz, F. R.; Capurro, C.; Durán, M.; East, G. A. Electropolymerization of N-vinylcarbazole in the presence of Galvinoxyl. *Polym. Bul.* **2006**, *57*, 321–328.

[32] Wang, X.; Lu, L. L.; Yu, Z. L.; Xu, X. W.; Zheng, Y. R.; Yu, S. H. Scalable template synthesis of resorcinol–formaldehyde/graphene oxide composite aerogels with tunable densities and mechanical properties. *Angew. Chem., Int. Ed.* **2015**, *54*, 2397–2401.

[33] Mulik, S.; Sotiriou-Leventis, C.; Leventis, N. Time-efficient acid-catalyzed synthesis of resorcinol–formaldehyde aerogels. *Chem. Mater.* **2007**, *19*, 6138–6144.

[34] Feng, C. Y.; Tang, L.; Deng, Y. C.; Wang, J. J.; Luo, J.; Liu, Y. N.; Ouyang, X. L.; Yang, H. R.; Yu, J. F.; Wang, J. J. Synthesis of leaf-vein-like g-C_3N_4 with tunable band structures and charge transfer properties for selective photocatalytic H_2O_2 evolution. *Adv. Funct. Mater.* **2020**, *30*, 2001922.

[35] Shiraishi, Y.; Kofuji, Y.; Sakamoto, H.; Tanaka, S.; Ichikawa, S.; Hirai, T. Effects of surface defects on photocatalytic H_2O_2 production by mesoporous graphitic carbon nitride under visible light irradiation. *ACS Catal.* **2015**, *5*, 3058–3066.

[36] Wang, Y. B.; Meng, D.; Zhao, X. Visible-light-driven H_2O_2 production from O_2 reduction with nitrogen vacancy-rich and porous graphitic carbon nitride. *Appl. Catal. B: Environ.* **2020**, *273*, 119064.

[37] Moon, G. H.; Fujitsuka, M.; Kim, S.; Majima, T.; Wang, X. C.; Choi, W. Eco-friendly photochemical production of H_2O_2 through O_2 reduction over carbon nitride frameworks incorporated with multiple heteroelements. *ACS Catal.* **2017**, *7*, 2886–2895.

[38] Li, S. N.; Dong, G. H.; Hailili, R.; Yang, L. P.; Li, Y. X.; Wang, F.; Zeng, Y. B.; Wang, C. Y. Effective photocatalytic H_2O_2 production under visible light irradiation at g-C_3N_4 modulated by carbon vacancies. *Appl. Catal. B: Environ.* **2016**, *190*, 26–35.

[39] Xiong, J.; Li, X. B.; Huang, J. T.; Gao, X. M.; Chen, Z.; Liu, J. Y.; Li, H.; Kang, B. B.; Yao, W. Q.; Zhu, Y. F. CN/rGO@BPQDs high-low junctions with stretching spatial charge separation ability for photocatalytic degradation and H_2O_2 production. *Appl. Catal. B: Environ.* **2020**, *266*, 118602.

[40] Samanta, S.; Yadav, R.; Kumar, A.; Sinha, A. K.; Srivastava, R. Surface modified C, O co-doped polymeric g-C_3N_4 as an efficient photocatalyst for visible light assisted CO_2 reduction and H_2O_2 production. *Appl. Catal. B: Environ.* **2019**, *259*, 118054.

[41] Zhou, L.; Feng, J. R.; Qiu, B. C.; Zhou, Y.; Lei, J. Y.; Xing, M. Y.; Wang, L. Z.; Zhou, Y. B.; Liu, Y. D.; Zhang, J. L. Ultrathin g-C_3N_4 nanosheet with hierarchical pores and desirable energy band for highly efficient H_2O_2 production. *Appl. Catal. B: Environ.* **2020**, *267*, 118396.